Earth and Planetary Science Letters 396 (2014) 125–133

Contents lists available at ScienceDirect

Earth and Planetary Science Letters

www.elsevier.com/locate/epsl

Nanopaleomagnetism of meteoritic Fe–Ni studied using X-ray photoemission electron microscopy

James F.J. Bryson [a,*], Julia Herrero-Albillos [b,c,d], Florian Kronast [e], Massimo Ghidini [f,g], Simon A.T. Redfern [a], Gerrit van der Laan [h], Richard J. Harrison [a]

[a] Department of Earth Sciences, University of Cambridge, Downing Street, Cambridge, CB2 3EQ, United Kingdom
[b] Fundación ARAID, Paseo María Agustín 36, E-50004 Zaragoza, Spain
[c] Centro Universitario de la Defensa, Ctra. de Huesca s/n, E-50090 Zaragoza, Spain
[d] Instituto de Ciencia de Materiales de Aragón, CSIC – Universidad de Zaragoza, Pedro Cerbuna 12, E-50009 Zaragoza, Spain
[e] Helmholtz Zentrum Berlin, Elektronenspeicherring BESSY II Albert-Einstein-Strasse 15, Berlin 12489, Germany
[f] Department of Material Sciences, University of Cambridge, Cambridge, CB3 0FS, United Kingdom
[g] DiFeST, University of Parma, viale G.P. Usberti 7/A, 43124 Parma, Italy
[h] Diamond Light Source, Chilton, Didcot, Oxfordshire, OX11 0DE, United Kingdom

ARTICLE INFO

Article history:
Received 21 January 2014
Received in revised form 4 April 2014
Accepted 7 April 2014
Available online 23 April 2014
Editor: J. Brodholt

Keywords:
extraterrestrial magnetism
tetrataenite
cloudy zone
high-resolution magnetic microscopy
X-ray photoemission electron microscopy

ABSTRACT

X-ray photoemission electron microscopy (XPEEM) enables natural remanent magnetisation to be imaged with ~ 30 nm resolution across a field of view of 5–20 μm. The method is applied to structural features typical of the Widmanstätten microstructure (kamacite – tetrataenite rim – cloudy zone – plessite) in the Tazewell IIICD iron meteorite. Kamacite lamellae and the tetrataenite rim are multidomain, whereas plessite consists of laths of different phases displaying a range of stable magnetisation directions. The cloudy zone (CZ) displays a complex interlocking domain pattern resulting from nanoscale islands of tetrataenite with easy axes distributed along three possible crystallographic directions. Quantitative analysis of the coarse and intermediate CZ was achieved using a combination of image simulations and histogram profile matching. Remanence information was extracted from individual regions of interest ~ 400 nm wide, demonstrating for the first time the capability of XPEEM to perform quantitative paleomagnetic analysis at sub-micron length scales. The three tetrataenite easy axis orientations occur with equal probability in the coarse and intermediate CZ, suggesting that spinodal decomposition in these regions was not strongly influenced by internal interaction fields, and that they are suitable candidates for future paleomagnetic studies. The fine CZ shows a strong dominance of one easy axis. This effect is attributed to island–island exchange interactions that render the fine CZ unsuitable for paleomagnetic study. Variations in the relative strength (proportion of dominant easy axis) and direction (direction of dominant easy axis) of a paleomagnetic field can be resolved from different regions of the CZ using XPEEM, raising the prospect of obtaining a time-resolved measurement of the active dynamo period in meteorites originating from the upper unmelted regions of differentiated asteroids (e.g. chondrites, pallasites, mesosiderites).

1. Introduction

Meteorites are our primary source of information regarding the magnetic fields generated billions of years ago by planetary bodies (Weiss and Elkins-Tanton, 2013). An increasing body of paleomagnetic evidence gathered from meteorites suggests that Mars (Weiss et al., 2008), the Moon (Garrick-Bethell et al., 2009) and many asteroids (Fu et al., 2012; Tarduno et al., 2012; Weiss and Elkins-Tanton, 2013) differentiated during the early stages of the solar system and generated dynamo fields with strengths comparable to that of present-day Earth. A logical progression from these studies is to measure the time dependence of these dynamo fields, which currently requires obtaining samples from a single body of different ages and deducing the field that magnetised each sample individually (Dwyer et al., 2011). A time-resolved asteroid dynamo record could provide insight into the processes of

* Corresponding author.
E-mail addresses: jfjb2@cam.ac.uk (J.F.J. Bryson), Julia.Herrero@unizar.es (J. Herrero-Albillos), florian.kronast@helmholtz-berlin.de (F. Kronast), mg526@cam.ac.uk (M. Ghidini), satr@cam.ac.uk (S.A.T. Redfern), gerrit.vanderlaan@diamond.ac.uk (G. van der Laan), rjh40@cam.ac.uk (R.J. Harrison).

http://dx.doi.org/10.1016/j.epsl.2014.04.016

core solidification and dynamo field decay, and thereby contribute significantly to our understanding of planetary evolution. It has recently been shown (Bryson et al., 2014) that time-resolved records of asteroid dynamos can potentially be encoded within spinodal nanostructures unique to meteoritic metal, termed the cloudy zone (CZ). Extracting this signal, however, requires paleomagnetic measurements to be made on the micrometer to sub-micrometer length scales. Currently this task is the beyond the capabilities of conventional imaging techniques employed in paleomagnetism. In this study we demonstrate a new approach based on synchrotron X-ray magnetic imaging that, combined with the unique properties of the CZ, allows quantitative analysis of nanoscale remanence and the potential to study the temporal evolution of asteroid dynamo fields.

X-ray photo-emission electron microscopy (XPEEM, Stohr et al., 1998) is a technique capable of imaging the surface magnetisation of a polished sample with a spatial resolution down to 30 nm and a 5–20 μm field-of-view. Unlike other techniques (e.g. electron holography, magnetic force microscopy, scanning magnetic microscopy) XPEEM produces a signal that is directly proportional to the local magnetic moment of the sample (rather than a signal that is proportional to the magnetic induction or external stray field created by the sample). This negates the need for complex inverse methods to recover the magnetisation, which is an underdetermined problem that can only be solved for very specific cases (e.g. for unidirectional magnetisation, Lima et al., 2013). Furthermore, XPEEM measurements can be performed without the need to expose the sample to strong fields either during measurement or sample preparation. These two unique properties of XPEEM allow for direct nanoscale paleomagnetic measurements of highly targeted regions of interest. XPEEM has been applied at low magnifications to the Gibeon IVA iron meteorite (Kotsugi et al., 2010). This meteorite experienced considerable shock reheating (Goldstein et al., 2009a), however, and hence does not contain a CZ. Here we apply XPEEM to the Tazewell IIICD iron meteorite, which contains unaltered CZ (Goldstein et al., 2009b). The CZ consists of conjoined, single domain islands of tetrataenite (FeNi) embedded in a matrix of Fe_3Ni (Leroux et al., 2000; Bryson et al., 2014). Each tetrataenite island can adopt one of six magnetisation directions as it forms, and the proportions of these six directions, averaged over a large enough number of islands, relates to both the intensity and direction of the field experienced by the CZ. As the CZ forms with increasing lateral distance over a period of 10–100 Myr, the local magnetisation relates to the temporal evolution of the dynamo field over this time period. Of the iron meteorite classes that have had their cooling rates measured with modern techniques, the IIICD meteorites are the most slowly cooled (Goldstein et al., 2013). Hence, the Tazewell is likely to have originated from the core or deep mantle of an asteroid, meaning it is unlikely to have cooled through the tetrataenite formation temperature while a putative core dynamo was active. This study therefore acts as a control for future measurements made on meteorites derived from shallower depths, whose CZs could potentially have formed in the presence of a dynamo field.

2. Methods

XPEEM (Fig. 1) involves illuminating a sample surface with a monochromatic beam of circularly polarised soft X-rays, with their energy tuned to the absorption edge of an element of interest (the Fe $L_{2,3}$ edge in this case). The circular polarisation of the photon introduces an angular momentum (Stohr, 1999) which can be transferred to an electron during excitation across the absorption edge. This transfer results in differing excitation probabilities depending on the direction of the electron magnetic moment relative

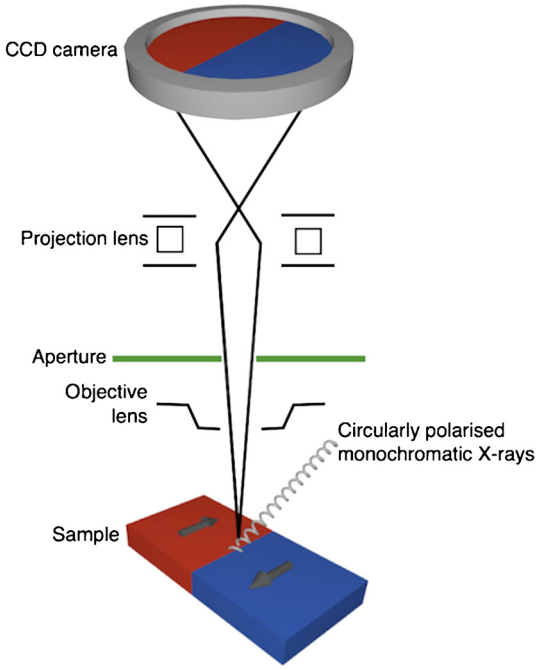

Fig. 1. Schematic of the XPEEM. Circularly polarised monochromatic X-rays illuminate a sample surface, which consists of antiparallel magnetic domains (blue and red). The secondary electrons ejected from the surface during excitation by these X-rays pass through the objective lens, aperture and projection lens to create a focused, magnified image of the magnetic pattern of the sample surface on a CCD camera placed above the sample. The spatial resolution and magnification are determined by the lenses and aperture.

to the direction of the X-ray beam (van der Laan, 2013). Secondary electrons that escape the sample surface are accelerated through a set of electron lenses to form a focused, magnified image of the magnetisation projected onto the X-ray beam direction (Nolting et al., 2000). This signal, I, is enhanced and normalised by measuring the XPEEM signal with opposite circular polarisations:

$$I = \frac{I_R - I_L}{I_R + I_L} \tag{1}$$

where I_R and I_L are the intensity measurements with right and left circularly polarised X-rays, respectively. Secondary electrons can escape from the top ~ 5 nm of a metallic sample (Ohldag et al., 2001), hence only the surface magnetic domain pattern is probed. The XPEEM measurements were performed at the SPEEM UE49 beamline at BESSY II, Berlin. The X-ray beam was orientated 16° out of the plane of the sample, making the XPEEM intensity sensitive to all three spatial components of the surface magnetisation. The spatial resolution of the images is limited by the optics in the secondary electron detector and stray fields originating from the sample itself, and was measured from the results in this study to be ~ 120 nm. A unique sample holder was used, capable of applying magnetic fields up to ~ 100 mT in the plane of the sample while images are captured with no loss of spatial resolution. The results were acquired with either 20 μm, 15 μm or 5 μm field of view.

A section of the Tazewell meteorite was acquired from the Sedgwick Museum of Earth Sciences, University of Cambridge, sample number 16 269. This meteorite was chosen based on previous transmission electron microscopy studies (Goldstein et al., 2009b; Reuter et al., 1987; Yang et al., 1997) demonstrating an abundance of the CZ. The sample was mechanically polished to provide the flat surface necessary for XPEEM. Polishing induces a

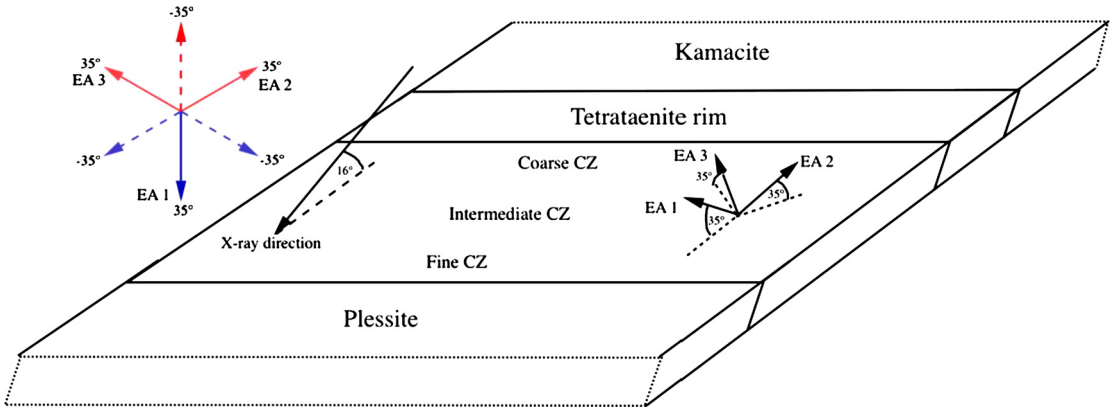

Fig. 2. Cartoon of the relative orientations of the microstructure, potential tetrataenite easy axes and the X-ray beam relating to Figs. 4, 5, 6, 7 and 8. The in-plane projection of the easy axes differ by 120°, and are 35° out of the plane of the sample. The X-ray beam is 16° out of the plane of the sample, with an in-plane component parallel to that of easy axis 1. The inset in the top left displays the easy axes viewed from above demonstrating both the positive and negative out-of-plane directions. The out-of-plane angle of each axis is included. Easy axes with a negative out-of-plane component are shown as dashed arrows. The colour of the XPEEM signal each easy axis will create is included as the arrow colour. (For interpretation of the references to colour in this figure, the reader is referred to the web version of this article.)

transition in the upper ~80 nm of the sample surface which generates a magnetically soft layer with a coercivity < 200 mT (see Supplementary material). This layer was completely removed by Ar ion sputtering under high vacuum (17.25 hours at decreasing voltages from 1.4 V to 0.5 V) allowing the underlying CZ to be studied. Electron diffraction results from the same sample (Bryson et al., 2014) demonstrate that the surface under investigation is orientated normal to a [111] zone axis. Thus, all three possible ⟨001⟩ tetrataenite easy axes were pointing 35° out of the sample surface (Fig. 2), with the in-plane component of one of the easy axes (easy axis 1) perpendicular to the tetrataenite rim and the other two easy axes ±120° different from this (easy axis 2 and 3 respectively). The sample had previously been used in magnetic force microscopy measurements (see Supplementary material) which involved the sample experiencing a 1 T field normal to the plane of the surface. This field will not have altered the easy axis distribution within the CZ, but will have caused a uniform out-of-plane moment alignment in tetrataenite islands with a coercivity < 1 T.

Quantitative analysis was performed by simulating model nanostructures designed to mimic the structural and magnetic properties of the CZ (see Appendix A). Models consisted of Voronoi cells (tetrataenite islands) embedded within a second continuous structure (matrix phase) with dimensions that matched those observed experimentally (Reuter et al., 1987). An easy axis and corresponding magnetisation component were assigned to each island and the matrix phase (based on representative values determined by micromagnetic simulation, see Supplementary material). We model the matrix magnetic signal as an induced magnetisation that depends on the neighbouring tetrataenite islands. The XPEEM image was then simulated by projecting the magnetisation onto the X-ray direction, convoluting with an approximation to the experimental point spread function, downsampling and then adding noise to the resulting image so the experimental and simulated results could be compared directly on a pixel-by-pixel basis. Histograms of the pixel intensity and size of the domains were calculated for both the experimental and simulated data. Both the proportion and extent of clustering of each easy axis were varied until the experimental and simulated histograms for both properties agreed. This analysis allowed for the easy axis distribution (long range order) and local interactions (short range order) present in the experimental images to be deduced quantitatively. This procedure was performed for the coarse (~80 nm diameter islands), intermediate (~40 nm diameter islands) and fine (< 20 nm diameter islands) CZ regions.

3. Results

3.1. Direct observations

Each pixel in an XPEEM image represents the average moment of a 10 nm × 10 nm × 5 nm volume projected onto the X-ray beam direction. Fig. 2 shows the relative orientations of the X-ray beam direction, the microstructural features and all three potential easy axes. The 1 T field applied to the sample before measuring is expected to induce a uniform positive out-of-plane component to the magnetisation within those regions of the CZ with a coercivity < 1 T. This magnetisation distribution is expected to generate two signals, as shown in the inset in Fig. 2: easy axis 1 will give rise to a large positive signal (blue); easy axes 2 and 3 will give rise to a negative signal with approximately half the intensity of that from easy axis 1 (red). A reversal of the out-of-plane component of the magnetisation along any given easy axis will result in a change of the signal from red to blue (or vice verse, see Fig. 2 inset).

The results reveal dramatic variations in the magnetic domain pattern across the kamacite, tetrataenite rim, CZ and plessite (Figs. 3 and 4a). The kamacite is clearly multidomain, displaying large domains that are easily manipulated with weak applied fields (see Supplementary material). The tetrataenite rim is also multidomain, displaying smaller domains with domain walls that mostly run parallel to the three possible easy axis orientations. Although these domains show negligible variations in position with the fields applied in the XPEEM, the rim is still unlikely to provide reliable paleomagnetic information due to its multidomain nature. Abrupt changes in the magnetic domain pattern at the interface between the kamacite and the tetrataenite rim are also observed, as expected given the large anisotropy contrast between these phases. The coarse CZ (Fig. 4b) displays a detailed and complex interlocking network of positive and negative domains. As the island diameter decreases in the intermediate CZ, the magnetic domain size decreases and the signal weakens. Given the magnetic history of the sample, the presence of blue and red regions is indicative of multiple easy axes within the coarse and intermediate CZ regions. As the fine CZ region is approached, the signal intensity increases, first adopting a relatively uniform red colour before abruptly reversing to a relatively uniform blue colour. The interface between the red and blue regions displays a rough texture and is parallel to the tetrataenite rim. The plessite displays detailed and elongated lath-like structures, although it is difficult to differentiate between the martensite and tetrataenite (Fig. 3). Both the CZ and the majority of the plessite remain constant in the fields

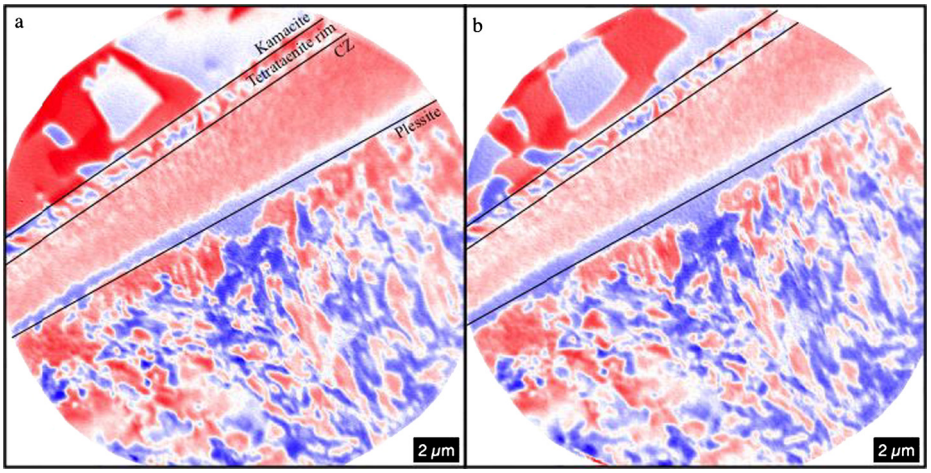

Fig. 3. (a) 20 μm field of view image of the kamacite, tetrataenite rim, CZ and plessite at remanence after zero applied field. (b) XPEEM image of the same area as (a) at remanence after an applied field of ∼ 100 mT in the plane of the sample. A significant rearrangement of the magnetic domains in the kamacite is observed with the applied field, but the tetrataenite rim and CZ are unaffected. Small parts of the plessite vary with the field, although the overall magnetisation pattern is largely retained. The boundaries between the phases are highlighted as solid black lines.

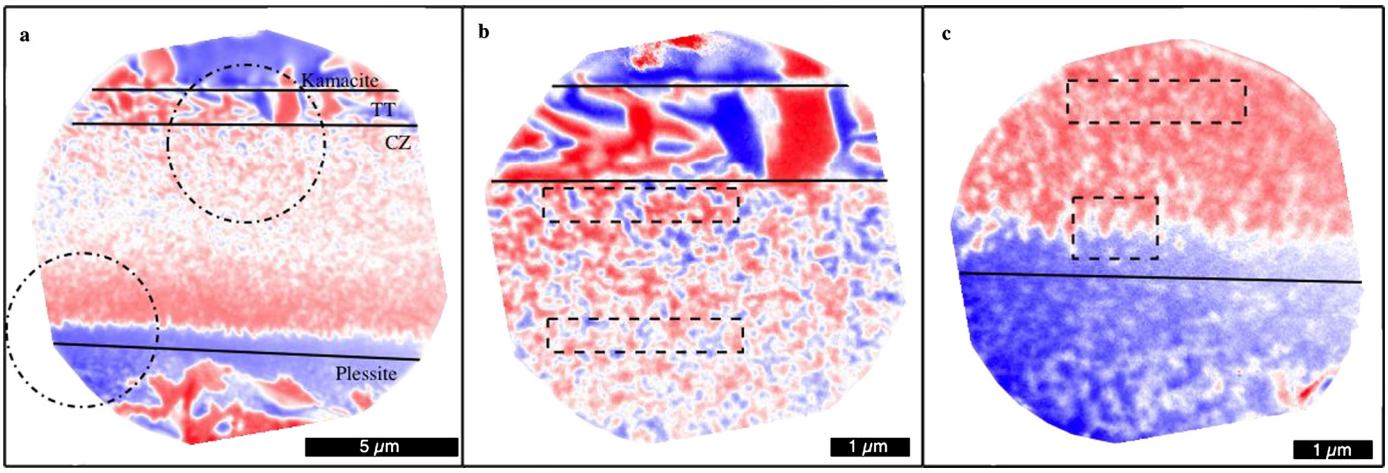

Fig. 4. (a) 15 μm field of view image of the kamacite, tetrataenite rim (TT), CZ and plessite. Interfaces between the phases have been marked with solid black lines. (b, c) 5 μm field of view image of the tetrataenite rim and coarse CZ, and fine CZ and plessite respectively marked by dashed circles in (a). Noise is visible in the kamacite at the top of (b) resulting from detector saturation. The dashed boxes in (b) and (c) correspond to the regions used in Figs. 5, 6, 7 and 8.

applied in the XPEEM (maximum of 100 mT), so have the potential to provide reliable paleomagnetic information (Fig. 3).

3.2. Quantitative analysis

Although the different easy axes give rise to signals that differ in both intensity and sign, it is not possible to assign local easy axes unambiguously to the CZ signal within the XPEEM images. This is because the resolution function of the XPEEM measurement is larger than the largest island diameter, meaning that the XPEEM signal is the average over several adjacent islands and the intervening matrix, which is predicted to have a saturation magnetisation value similar to that of tetrataenite (James et al., 1999). These effects are exemplified in Fig. A1, which clearly shows that the measured XPEEM signal relates to, but is not a direct mirror of, the magnetic state of the underlying CZ islands. These effects are most pronounced among the smaller tetrataenite islands, although are present throughout the entire CZ.

It is possible, however, to infer the easy axis distribution by simulating XPEEM images from idealised, model nanostructures and comparing pixel-intensity and domain-size histograms from the simulated and experimental images (Appendix A). The simulated nanostructures are not identical to those studied experimentally, but displayed both qualitative and quantitative similarities (e.g. island size and separation) such that, over a large enough area (approximately 3 μm × 400 nm in this case), the statistical distribution of experimental and simulated intensities are comparable. Simulating the histograms accounts for the difficulties mentioned above (resolution and matrix phase), providing a reliable method of quantitative comparison between the simulated and experimental data. Two variables were included in the simulations to enable the best agreement between simulated and experimental data to be achieved: the proportions of each easy axis (long range order) and the tendency to form clusters of the same easy axis direction (short range order).

For the coarse region (Fig. 5), the best histogram agreements are created with equal proportions of each of the three easy axes (i.e. 33% chance of an island displaying any one of the easy axes). The islands were populated with a degree of clustering (probability varied by a maximum of ±17%, depending on the magnetic state of the neighbouring islands) superimposed on a random easy axis distribution. The proportions could be changed by ±4% without a significant variation to the quality of fit between the experimental and simulated pixel intensity histograms, providing an estimate of the error. The pixel-intensity histograms (Fig. 5c) display an asymmetric peak with a steeper gradient among the negative values.

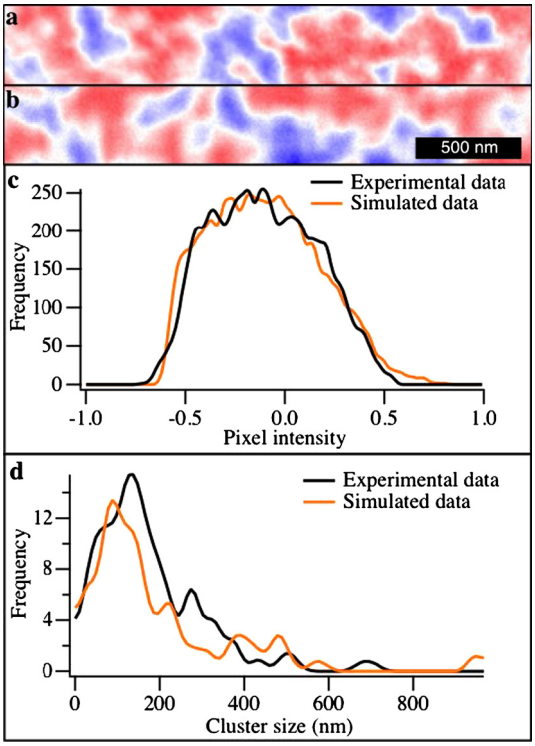

Fig. 5. Coarse region histogram analysis. (a) Experimental coarse CZ taken from Fig. 4(b). (b) Simulated coarse CZ XPEEM signal created with equal amounts of all three easy axis arranged with a degree of clustering atop a random distribution. The images in (a) and (b) display similarities in the size, shape and intensity of the domain pattern. (c) Pixel-intensity histograms of (a) and (b). The simulated and experimental curves agree well in peak position and shape. (d) Domain-size histogram of (a) and (b). The position and pattern of the main peaks agrees well between the two data sets. The easy axis distribution in the simulated data was the only way to recreate both sets of histograms.

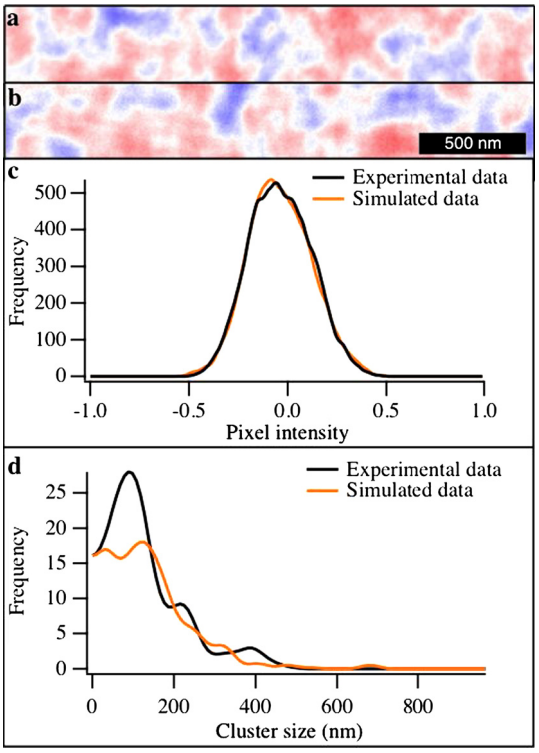

Fig. 6. Intermediate region histogram analysis. All parts correspond to those in Fig. 5. There is overall good agreement between the simulated and experimental data. The simulated data consisted of all three easy axis in close to equal proportions and a similar degree of clustering to that of Fig. 5 atop a random easy axis distribution.

Given the simulated nanostructure is composed mostly of a bimodal distribution of magnetisations, it is somewhat surprising that the resulting pixel-intensity histogram displays a single peak at a value close to zero. This observation is explained by the resolution of the XPEEM. Given the random distribution of the easy axes among the islands, convolving the simulated XPEEM signal with the experimental point spread function results in the averaging of the signal from positive and negative regions, creating pixels with intensities closer to zero. The asymmetry in the histogram results from the proportions of the easy axes and their relative XPEEM intensities. Both domain-size histograms (Fig. 5d) display a large peak at 100–150 nm and a decreasing number of larger domains up to 600–700 nm.

For the intermediate CZ (Fig. 6) the experimental and simulated histograms displayed the best agreement with $38\% \pm 4\%$ of the islands with easy axis 1, $62\% \pm 4\%$ of the islands with easy axis 2 and 3, and a similar degree of clustering to that of the coarse CZ. The pixel-intensity histogram (Fig. 6c) for this region is narrower than of the coarse region, and is still slightly asymmetric with a negative peak position. This narrower peak results from the smaller island diameter in this region. Upon convolution with the experimental point spread function, the signal from multiple islands are averaged resulting in increased cancellation compared to the coarse region. The peak position is, again, the result of the proportions of each of the easy axes. The domain-size histograms (Fig. 6d) both show dominant peaks at ~ 100 nm with fewer larger domains up to ~ 400 nm. Within the error of the model, the proportions of the easy axes and extent of clustering are very close to those derived for the coarse region.

As the fine CZ signal was entirely negative, it was not possible to generate the domain-size histograms, although a similar degree of clustering as observed in the previous two regions was required to produce good agreement between experimental and simulated pixel-intensity histograms. The experimental region used to create the histogram was taken from the top of Fig. 4c to reduce the chance of including islands with a negative out-of-plane component closer to the magnetic domain wall. The intensity histogram was best recreated with $92\% \pm 4\%$ of the easy axis 2 or 3 and $8\% \pm 4\%$ of easy axis 1 (Fig. 7). The pixel-intensity histogram (Fig. 7c) for this region is centred at -0.35 and is once again slightly asymmetric, with a steeper gradient at more negative values. This asymmetry is recreated in the simulations by the presence of clusters of islands with easy axis 1. The derived easy axis proportions are a significant departure from those drawn from the coarse and intermediate CZ.

Finally the pixel-intensity histogram for the rough interface in the fine CZ was simulated. The interface was modelled as a magnetic domain wall, with the probability of island reversal dictated by a tanh function of width 0.4 μm. The position of the interface was varied sinusoidally across the simulation to mimic the rough interface observed experimentally. There is a good agreement between the experimental and simulated histograms for this model with the same easy axis proportions as those used in the regular fine CZ (92% easy axis 2 or 3, and 8% easy axis 1, Fig. 8). The intensity histogram in this region is bimodal with peaks at ± 0.28 (Fig. 8c). The intensity histogram could only match the experimental curves by introducing sinusoidal variations along the length of the interface. This result implies that the interface is roughly 0.4 μm wide and that the data can be recreated with the same easy axis proportions for the entire fine CZ.

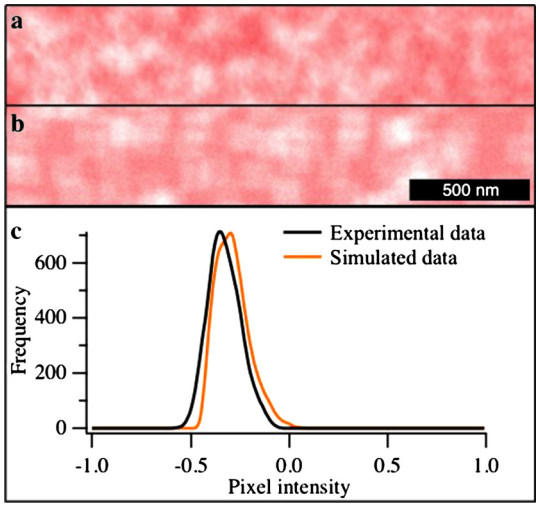

Fig. 7. Fine region histogram analysis. (a) Experimental fine CZ taken from Fig. 4(c). (b) Simulated fine CZ created with a significant dominance (92%) of easy axis and a similar degree of clustering as observed in Figs. 5 and 6. (c) Pixel-intensity histogram of (a) and (b). The agreement in shape between the two curves is excellent and the position of the curves is very similar.

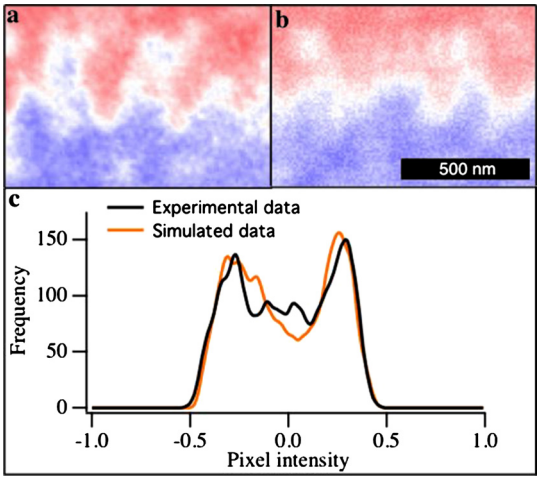

Fig. 8. Wall region histogram analysis. All parts correspond to those of Fig. 7. The simulated data was created with the same easy axis proportions as in Fig. 7, with a magnetic domain wall introduced with thickness 0.4 μm and a position that varied sinusoidally across the simulation. The overall good agreement between the curves demonstrates that the entire fine CZ can be simulated with the same easy axis distribution and that the reversal in the sign of the signal in the finest CZ corresponds to a reversal of magnetisation direction.

4. Discussion

The easy axis proportions drawn from the coarse and fine CZ are in excellent agreement with previous electron holography results of the same meteorite (Bryson et al., 2014). The XPEEM results greatly extend the field-of-view, however, allowing us to resolve the changing signals across the entire CZ. The histogram comparisons (Figs. 5, 6, 7 and 8) show that the coarse and intermediate CZ contain roughly equal proportions of the three easy axes among the tetrataenite islands, while there is strong mutual alignment of easy axes among islands in the fine CZ. The coarse and intermediate CZ fitting parameters suggest that the easy axes originally populated the islands at random, and as the nanostructure evolved, larger clusters of the same easy axis formed without changing the overall proportions. This likely results from a process of Ostwald ripening, with small domains of one easy axis shrinking at the expense of larger domains of an alternate easy axis. This process accounts for both the observed equal proportions of all three easy axes and the cluster size.

The presence and position of the magnetic domain wall in the fine CZ can be understood by considering the coercivity variations across the CZ. The coercivity has been observed to vary from ~ 0.4 T to > 1 T with increasing lateral distance across the CZ (Uehara et al., 2011). The decrease in coercivity from the intrinsic tetrataenite value is the result of the exchange interaction with the magnetically-soft matrix (Kneller and Hawig, 1991). The strength of this effect decreases as the matrix width decreases (Asti et al., 2004). The observed magnetic domain wall represents a 1 T contour, separating the CZ into regions above the wall (predominantly red signal) with a coercivity < 1 T, from a region below the wall (predominantly blue signal) with a coercivity > 1 T. The roughness in this 1 T contour is presumably the result of local variations in the matrix thickness, which result in small-scale (< 100 nm) variations in coercivity of the fine CZ.

We attribute the strong alignment of easy axes in the fine CZ to a fundamental change in magnetic regime, linked to chemical and structural differences between this region and the rest of the CZ. Reuter et al. (1987) observed a second rim in light microscopy measurements of the IIICD iron meteorites between the CZ and plessite. These authors speculate about the structure of this rim, and suggest it should be predominantly (possibly completely) matrix phase. We observe a hard and non-uniform magnetic signal in this region, however, suggesting that tetrataenite is also present, most likely as very small islands. TEM studies show that the matrix phase in the fine region is very narrow. According to the theory of hard/soft nanocomposites, when the width of the matrix phase decreases below a critical value, the system may change from the 'exchange spring' regime characteristic of the course and intermediate CZ to a 'rigid magnet' regime (Asti et al., 2004). In the rigid magnet regime, the matrix moments become rigidly coupled to the hard phase, allowing exchange interactions between adjacent islands to propagate through the matrix, leading to enhanced alignment in the magnetisation direction. A change in magnetic regime of this nature is consistent with both the dramatic increase in easy axis alignment and the enhanced coercivity of the fine CZ. We suggest that the signal observed in the fine CZ is an intrinsic property of this region, rather than the result of CZ formation in an external field. The fine CZ should not, therefore, be used in paleomagnetic studies. Roughly half of the CZ could experience this effect, hence reducing the dynamo field time-period that can be studied reliably to 5–50 Myr depending on the cooling rate of the meteorite.

The histogram comparisons (Figs. 5, 6, 7 and 8) show a degree of short range order in all regions studied. This likely originates from either local stray fields created by the nanostructure itself (i.e. the field generated by an island influencing the orientation of its neighbours), or natural coarsening during spinodal decomposition, such that small islands with one easy axis orientation are eliminated in favour of larger islands of a different orientation. Although stray fields are unlikely to have profound effects over large distances, local stray fields could influence the easy axis distribution. Simulations of the evolution of spinodal microstructures (Chen, 1993, 1994; Seol et al., 2003) show that specific spinodal microstructures can form and reduce the energy of unmixing (e.g. alternating islands of different ordered end members), which could result in the clustering observed in this study (in this case preferential clustering of islands with the same lattice orientation). At this stage we can only speculate about the origin of clustering, and note the possibility that magnetic fields could have a slight effect on the coarse and intermediate CZ magnetisation, albeit at a small length scale (100–200 nm). Spinodal decomposition simulations using a free energy expression representing the CZ are needed to identify the source of the clustering.

A limited amount of experimental work has been performed on tetrataenite (especially as a component of the CZ), as it is only observed in nature in meteorites. Little is known for certain about how magnetic fields of various intensities influence the proportions of easy axes in the CZ. However, it is physically reasonable to assume that, in the absence of any external influence, all three easy axes (and six magnetisation directions) are expected to be present with equal probability among the tetrataenite islands (Dunlop and Ozdemir, 1997). This easy axis distribution is observed in the coarse and intermediate CZ (Figs. 5 and 6), implying there were no external influences acting on these regions during CZ formation. The most likely external influence for these two regions would have been stray magnetic fields from adjacent regions. The most likely source of stray fields in the coarse and intermediate CZ is the kamacite and tetrataenite rim, both of which are multidomain (Fig. 4a). Domain walls are able to move freely to reduce the stray magnetic fields emanating from these regions (unlike those in the plessite, which are controlled by the underlying lath structure). This may explain the lack of stray field experienced by the CZ (Dunlop and Ozdemir, 1997). The implication is that the CZ will display all three easy axes with equal probability unless it experiences a field (or other interactions) that biases one direction over the others.

Previous studies have shown that chondrites, pallasites and mesosiderites can contain the CZ (Uehara et al., 2011; Reuter et al., 1987; Yang et al., 1997). If these meteorites originated from the outer (unmelted) regions of an otherwise differentiated asteroid (e.g. as a result of incremental accretion or impacts, Weiss and Elkins-Tanton, 2013; Tarduno et al., 2012; Greenwood et al., 2006), it is possible that the metal in these meteorites was cool enough to acquire a remanent magnetisation while the core dynamo was still active. Tetrataenite islands form progressively over a period of around 10–100 Ma with increasing lateral distance across the CZ (Goldstein et al., 2009b). By exploiting this time- and position-dependence to the magnetisation acquisition, dynamo field variations over this time period can be deduced from XPEEM measurements of the proportions of possible magnetisation directions across the CZ width. The results of this study show that any deviations from an equal population of magnetisation directions in the coarse and intermediate CZ can be attributed to an external field and used to study the temporal evolution of dynamo fields. The same analysis technique employed in this study could easily be transferred to other classes of metal-bearing meteorites, and will allow both the strength (extent of deviation from random state) and relative direction (predominant direction of the CZ islands) of the dynamo field to be calculated.

5. Conclusions

We have demonstrated the potential of XPEEM to perform paleomagnetic measurements on sub-micrometer length scales in meteoritic metal. The method was used to show that the CZ in the Tazewell IIICD iron meteorite contains equal proportions of the possible easy axes among the coarser and intermediate sized islands. This observation implies that these regions did not experience a field as they formed. The fine CZ displays a significant bias of one easy axis direction. This effect is attributed to the small size of the matrix phase in this region, which transmits the direct exchange interactions between neighbouring islands. The fine CZ is, therefore, a poor paleomagnetic recorder, as its strong magnetisation is caused by an inherent property of the CZ rather than the external field. This feature could effect half of the CZ width. The coarse and intermediate CZ islands, however, could provide information about the temporal evolution of the dynamo field generated by their parent body, encoded as the spatial variations in proportions of islands with each of the six possible magnetisation directions. XPEEM is currently the only method with the combination of high spatial resolution, wide field of view and capability to study the magnetisation directly that enable such measurements to be made.

Appendix A

To create the simulated XPEEM images, model nanostructures were first generated via a Voronoi construction. A 1024×512 simulation cell with 2.5 nm resolution was divided into 800 equal sized squares, and a single pixel within each square was then chosen at random. Voronoi cells were constructed around each of these pixels. These cells were then eroded to generate islands embedded within a matrix (Fig. A1a). This process created islands with a range of diameters, with the majority close to 80 nm, matching experimental images (Bryson et al., 2014). An easy axis was then assigned to each island. The probability of an island adopting a certain easy axis was dependent upon the predefined proportions of each easy axis (i.e. a 1/3 chance of an island adopting any of the 3 easy axes for an equal random distribution). To model the clustering of neighbouring easy axes, the probability of each easy axis was modified depending the magnetisation of the neighbouring islands, such that it was favourable for an island to adopt the same easy axis direction as the majority of its neighbouring islands. The mathematical description of the probability, P_i, of an island adopting an easy axis i, is as follows:

$$P_i = A_i + \frac{1}{B}\sum_{j=1}^{5} M_j \tag{A.1}$$

where A_i is the predefined proportion of easy axis i, B is a measure of the extent of clustering ($B = 30$ for all simulations in this study) and M_j is the reduced magnetisation of the jth. nearest neighbouring island (as the majority of islands had 5 nearest neighbours this was the maximum number of neighbouring islands studied), which adopts a value of $+1$ if the projection of the magnetisation onto the y direction is positive, 0 if the projected magnetisation is zero, and -1 if the projected magnetisation is negative. The islands were populated with easy axes sequentially, down the pixel columns. Corresponding magnetisation values were then assigned to the islands and matrix phase. These magnetisation values were based on the results of micromagnetic simulations. In these simulations, it was observed that the magnetisation direction of the matrix adopted one of a set of possible values depending on the magnetisation direction of the two islands that locally encased the matrix region. This dependence in the matrix magnetisation was implemented into the model magnetic nanostructures. Given the X-ray direction was parallel to the y direction in the simulations and slightly out-of-plane, only the y (Fig. A1b) and z (Fig. A1c) components of the magnetisation were required to create the XPEEM image (Fig. A1d), which is the projection of the magnetisation onto the X-ray direction. The XPEEM signal was then blurred using a 120 nm $\times$ 120 nm square convolution kernel (matching the size of the experimental point spread function as deduced by studying the measured wall width in the tetrataenite rim) to simulate the resolution achieved experimentally (Fig. A1e). The resulting image was then downsized to 10 nm per pixel to match the experimental image sampling. Random noise was then added to the results (Fig. A1f). Pixel-intensity histograms were then generated from the experimental and the final simulated data sets. The pixel-intensity histogram was normalised with respect the XPEEM intensity observed in the tetrataenite rim, where the domains were large enough to not have experienced intensity reduction due to the resolution of the XPEEM. The domain-size histograms were created by measuring the length of any region with negative intensity for each pixel row. The results of this analysis

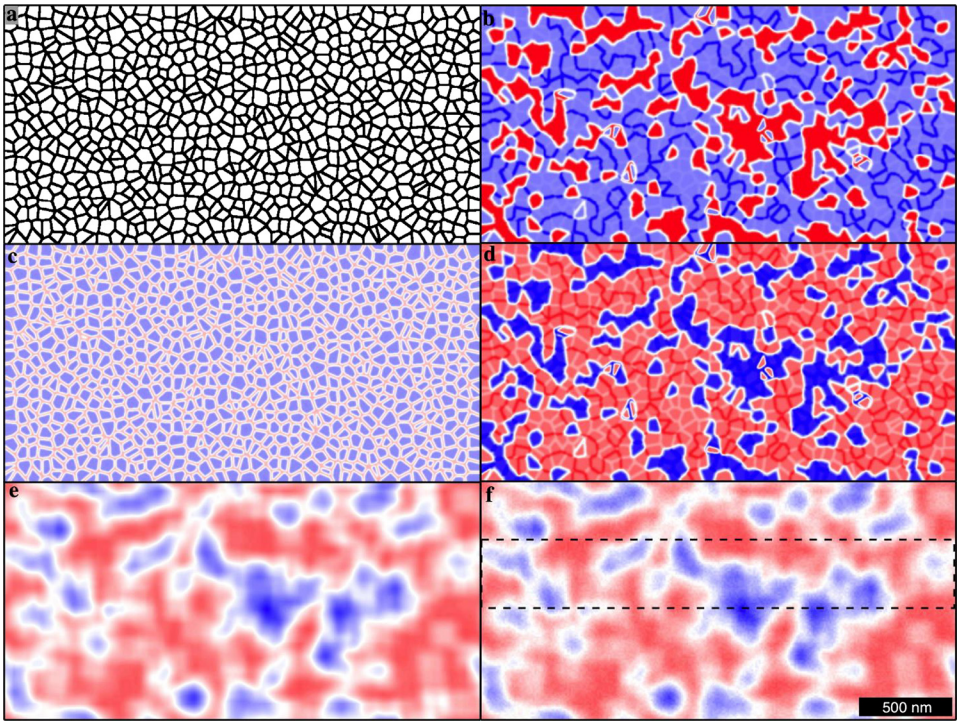

Fig. A1. (a) Representative model nanostructure of the coarse CZ created by eroding Voronoi cells constructed upon a constrained random distribution of points. (b, c) *y* and *z* components of the magnetisation respectively. The island easy axis distribution is based on an equally populated random distribution, modified by the magnetisation of neighbouring islands to introduce a degree of clustering. (d) XPEEM signal generated by projecting the magnetisation components onto the X-ray direction. The in-plane component of this direction is parallel to the *y* direction of the simulation cell, and is 16° out-of-plane. (e) XPEEM signal after having been blurred by a square 120 nm × 120 nm convolution kernel. (f) XPEEM signal after having been down sampled so each pixel is 10 nm and random noise added, so the experimental and simulated images could be compared. The dashed box represents the area in Fig. 5a.

were very similar for pixel columns and rows, hence only the row analysis results have been included. This process was repeated for the intermediate and fine CZ, by subdividing the simulation cell into 3200 and 12 800 equally sized squares, respectively.

As can be seen in Fig. A1d & f, the XPEEM signal is representative of the island magnetisation, although it is by no means an exact copy. Hence it is not valid to assign unambiguously easy axis directions to the experimental XPEEM images. This extent of this effect increases with the decreasing island size. Despite these difficulties, the simulated and experimental XPEEM images (e.g. Fig. 5a & b) clearly display qualitative similarities (in the shape, size and intensity of the domains) such that these two images can be compared statistically. As the simulated model nanostructures are not exact duplicates of reality, the comparisons between simulation and experiment must come from the histograms, which study the general properties of the images, and not the specific magnetic configuration.

Appendix B. Supplementary material

Supplementary material related to this article can be found online at http://dx.doi.org/10.1016/j.epsl.2014.04.016.

References

Asti, G., Solzi, M., Ghidini, M., Neri, F.M., 2004. Micromagnetic analysis of exchange-coupled hard-soft planar nanocomposites. Phys. Rev. B 69 (17), 174401.

Bryson, J.F.J., Church, N.S., Kasama, T., Harrison, R.J., 2014. Nanomagnetic intergrowths in Fe–Ni meteoritic metal: the potential for time-resolved records of planetesimal dynamo fields. Earth Planet. Sci. Lett. 388, 237–248.

Chen, L.-Q., 1993. A computer simulation technique for spinodal decomposition and ordering in ternary systems. Scr. Metall. Mater. 29, 683–688.

Chen, L.-Q., 1994. Computer simulation of spinodal decomposition in ternary systems. Acta Metall. Mater. 42 (10), 3503–3513.

Dunlop, D.J., Ozdemir, O., 1997. Rock Magnetism: Fundamentals to Frontiers. Cambridge University Press.

Dwyer, C.A., Nimmo, F., Stevenson, D.J., 2011. A long-lived lunar dynamo driven by continuous mechanical stirring. Nature 479, 212–214.

Fu, R.R., Weiss, B.P., Shuster, D.L., Gattacceca, J., Grove, T.L., Suavet, C., Lima, E.A., Li, L., Kuan, A.T., 2012. An ancient core dynamo in asteroid Vesta. Science 338 (6104), 238–241.

Garrick-Bethell, I., Weiss, B.P., Shuster, D.L., Buz, J., 2009. Early lunar magnetism. Science 323, 356–359.

Goldstein, J., Yang, J., Kotula, P., Michael, J., Scott, E., 2009a. Thermal histories of IVA iron meteorites from transmission electron microscopy of the cloudy zone microstructure. Meteorit. Planet. Sci. 44 (3), 343–358.

Goldstein, J.I., Scott, E.R.D., Chabot, N.L., 2009b. Iron meteorites crystallization, thermal history, parent bodies, and origin. Chem. Erde – Geochem. 69 (4), 293–325.

Goldstein, J.I., Scott, E.R.D., Winfield, T., Yang, J., 2013. Thermal histories of group IAB and related iron meteorites and comparison with other groups of irons and stony iron meteorites. In: 44th Lunar and Planetary Science Conference.

Greenwood, R.C., Franchi, I.A., Jambon, A., Barrat, J.A., Burbine, T.H., 2006. Oxygen isotope variation in stony-iron meteorites. Science 313, 1763–1765.

James, P., Eriksson, O., Johansson, B., Abrikosov, I.A., 1999. Calculated magnetic properties of binary alloys between Fe, Co, Ni, and Cu. Phys. Rev. B 59 (1), 419–429.

Kneller, E.F., Hawig, R., 1991. The exchange-spring magnet: a new material principle for permanent magnets. IEEE Trans. Magn. 27 (4), 3588–3600.

Kotsugi, M., Mitsumata, C., Maruyama, H., Wakita, T., Taniuchi, T., Ono, K., Suzuki, M., Kawamura, N., Ishimatsu, N., Oshima, M., Watanabe, Y., Taniguchi, M., 2010. Novel magnetic domain structure in iron meteorite induced by the presence of $L1_0$-FeNi. Appl. Phys. Express 3 (1), 013001.

Leroux, H., Doukhan, J.C., Perron, C., 2000. Microstructures of metal grains in ordinary chondrites: implications for their thermal histories. Meteorit. Planet. Sci. 35, 569–580.

Lima, E.A., Weiss, B.P., Baratchart, L., Hardin, D.P., Saff, E.B., 2013. Fast inversion of magnetic field maps of unidirectional planar geological magnetization. J. Geophys. Res., Solid Earth 118, 2723–2752.

Nolting, F., Scholl, A., Stohr, J., Seo, J., Fompeyrine, J., Siegwart, H., Locquet, J.-P., Anders, S., Luning, J., Fullerton, E., Toney, M., Scheinfein, M., Padmore, H., 2000. Direct observation of the alignment of ferromagnetic spins by antiferromagnetic spins. Nature 405, 767–769.

Ohldag, H., Regan, T., Stöhr, J., Scholl, A., Nolting, F., Lüning, J., Stamm, C., Anders, S., White, R., 2001. Spectroscopic identification and direct imaging of interfacial magnetic spins. Phys. Rev. Lett. 87 (24), 247201.

Reuter, K., Williams, D., Goldstein, J., 1987. Low temperature phase transformations in the metallic phases of iron and stony-iron meteorites. Geochim. Cosmochim. Acta 52, 617–626.

Seol, D., Hu, S., Li, Y., Shen, J., Oh, K., Chen, L., 2003. Computer simulation of spinodal decomposition in constrained films. Acta Mater. 51, 5173–5185.

Stohr, J., 1999. Exploring the microscopic origin of magnetic anisotropies with X-ray magnetic circular dichroism (XMCD) spectroscopy. J. Magn. Magn. Mater. 200, 470–497.

Stohr, J., Padmore, H., Anders, S., Stammler, T., Scheinfein, M., 1998. Principles of X-ray magnetic dichroism spectromicroscopy. Surf. Rev. Lett. 5 (6), 1297–1308.

Tarduno, J.A., Cottrell, R.D., Nimmo, F., Hopkins, J., Voronov, J., Erickson, A., Blackman, E., Scott, E.R.D., Mckinley, R., 2012. Evidence for a dynamo in the main group pallasite parent body. Science 338 (6109), 939–942.

Uehara, M., Gattacceca, J., Leroux, H., Jacob, D., van der Beek, C.J., 2011. Magnetic microstructures of metal grains in equilibrated ordinary chondrites and implications for paleomagnetism of meteorites. Earth Planet. Sci. Lett. 306 (3–4), 241–252.

van der Laan, G., 2013. Applications of soft X-ray magnetic dichroism. J. Phys. Conf. Ser. 430, 012127.

Weiss, B.P., Elkins-Tanton, L.T., 2013. Differentiated planetesimals and the parent bodies of chondrites. Annu. Rev. Earth Planet. Sci. 41 (1), 529–560.

Weiss, B.P., Fong, L.E., Vali, H., Lima, E.A., Baudenbacher, F.J., 2008. Paleointensity of the ancient martian magnetic field. Geophys. Res. Lett. 35 (23), L23207.

Yang, C.-W., Williams, D.B., Goldstein, J.I., 1997. A new empirical cooling rate indicator for meteorites based on the size of the cloudy zone of the metallic phases. Meteorit. Planet. Sci. 32, 423–429.